Corrosion Science 195 (2022) 109963

Contents lists available at ScienceDirect

Corrosion Science

journal homepage: www.elsevier.com/locate/corsci

Effect of variation in oxygen concentration in static Pb–Bi eutectic on long-term corrosion performance of Al-alloyed austenitic steels at 500 °C

Valentyn Tsisar [a,*], Erich Stergar [a], Serguei Gavrilov [a], Wouter Van Renterghem [a], Pierre Louette [b], Stéphane Lucas [b]

[a] Belgian Nuclear Research Centre SCK•CEN, Boeretang 200, Mol B-2400, Belgium
[b] University of Namur, Rue de Bruxelles, 61, B-5000 Namur, Belgium

ARTICLE INFO

Keywords:
A. Steel
Liquid metal
C. Oxidation
Leaching
Corrosion

ABSTRACT

Aluminium-alloyed austenitic steels Fe-14Cr-2Mn-20Ni-0.5Cu-3Al and Fe-14Cr-5Mn-12Ni-3Cu-2.5Al were tested at 500 °C in static Pb-Bi eutectic for 10,000 h. The concentration of oxygen in the liquid metal was changed in a controlled way over the course of the test from ~10^{-6} to ~10^{-9} mass% which provided conditions for oxidation and dissolution, respectively. Both steels showed slight oxidation of surface. Steel with higher Ni content revealed also initiation of dissolution corrosion in the view of rare pit-type damages. The structural and compositional features of oxide films, sub-oxide zones and corrosion damages are discussed.

1. Introduction

Alumina-Forming Austenitic steels (AFA), with improved creep and oxidation resistance for high temperature application in gaseous media [1–4], are also in focus for use in novel nuclear reactors with heavy-liquid metal coolants (HLM: Pb, Pb-Bi) that requires experimental studies on their compatibility.

Austenitic steels exclude Liquid-Metal Embrittlement (LME), the phenomenon which is of high concern for ferritic/martensitic steels (F/M) with a body-centered cubic structure [5]. However, conventional austenitic steels (not alloyed by Al) can undergo marked leaching of Ni, Mn, Cr, Fe etc. when contacting HLM at temperatures higher than 400 °C, which is one of the critical issues on the way of mastering HLM as a cooling media of next generation energetic facilities [6]. Selective leaching of the austenite stabilizers such as Ni and Mn results in phase transformation from austenite to ferrite in the corrosion zone. Leaching of steel constituents is accompanied by inverse penetration of the liquid metal into the steel matrix [7]. It results in a substantial corrosion loss which increasing with temperature due to the increase in solubility of the main steel constituents in the liquid metal.

A certain amount of oxygen in the liquid metal might change the interaction mode from dissolution to oxidation resulting in the formation of an oxide layer on the surface of the solid metal which operates as a mass-transfer barrier [8,9]. In-situ doping of liquid metal with oxygen is considered as a main approach to mitigate dissolution corrosion. Oxidation kinetics, morphology and composition of the oxide layer depend on the concentration of oxygen in the liquid metal. When the oxygen concentration is close to saturation, a thick bilayer magnetite scale is formed on the surface of austenitic steels [10]. It consists mainly of an outer magnetite (Fe_3O_4) layer formed on the side of the liquid metal and an inner Cr-deficient spinel $Fe(Fe,Cr)_2O_4$ layer formed on the side of the steel matrix. The upper part of the outer oxide with columnar structure is composed of plumboferrite [10]. Chromium in the inner spinel tends to be enriched at the grain boundaries while nickel is not bound by oxygen and forms non-oxidized islands inside the inner spinel [11,12].

At "working" concentrations of oxygen in the liquid-metal systems, which ranging from about 10^{-7} to 10^{-6} mass% and at temperatures 400–600 °C, the surface of austenitic steels is oxidized with formation of a very thin Cr-rich oxide film ($\leq$ 1 μm) reflecting incubation time and a thicker Fe–Cr oxide which characterizes accelerated oxidation [13–17]. Oxide layers, however, tend to degrade with time followed by the localized dissolution corrosion in spite of the high oxidation potential of the liquid metal body [14,16]. Therefore, the long-term durability of in-situ formed oxide layers is a weak point of the technology which is based on adding and continuous monitoring of oxygen concentration in the HLM.

The protective properties of an oxide film might be improved, similar to gaseous media, by means of alloying of the steel with elements which have a high affinity to oxygen (Si, Cr, Mn, Al etc.). Thus, Si-alloyed

* Corresponding author.
E-mail address: valentyn.tsisar@sckcen.be (V. Tsisar).

https://doi.org/10.1016/j.corsci.2021.109963
Received 24 August 2021; Received in revised form 15 November 2021; Accepted 16 November 2021
Available online 24 November 2021

austenitic and ferritic/martensitic (F/M) steels show improved oxidation resistance in oxygen-controlled HLM. The F/M steel EP823 is an example for a steel alloyed by Si (up to 3 wt%) in order to improve the corrosion resistance in HLM [8]. It should be underlined, that alloying with silicon does not change the morphology of the formed oxide, i.e. the typical bilayer Fe-based scale is formed as-well, but only the scale thickness decreases in comparison with steels of similar composition without Si-alloying [18]. Silicon, similar to Cr, is detected in the composition of the inner spinel layer and inner oxidation zone (IOZ). A very intensive development of an IOZ was observed on the Si-alloyed 1.4718 F/M steel (Fe-9Cr-3Si mass%) exposed to flowing Pb-Bi eutectic with 10^{-6} mass% dissolved oxygen for 15,028 h [19]. Excellent corrosion resistance of Si-containing austenitic steel 18Cr–20Ni–5Si at 450 and 550 °C in oxygen-saturated Pb–Bi for 3000 h was reported [20]. The surface of the steel was protected by an oxide film composed of Si and O preventing the dissolution of Ni and Cr into Pb–Bi which was observed on steels not alloyed by Si.

As regard the austenitic steels alloyed by aluminum, there are only few works reporting their corrosion behavior in lead-based melts. When the concentration of oxygen in static Pb-Bi eutectic is relatively high (5×10^{-4} mass%), the Fe-14Cr-25Ni-3.5Al-2Mn-2Mo-2.5Nb alloy shows intensive oxidation at 520 °C [21]. An exposure of 1850 h resulted in the formation of a thick bilayer magnetite scale [21]. This result is very similar to those demonstrated by the conventional austenitic steels, not alloyed by Al [10], and indicates about no significant gain in oxidation resistance for Al-alloyed austenitic steels in HLM with high oxidation potential. However, when the oxygen concentration was decreased to 10^{-6} mass%, a thin protective oxide film, composed of Cr_2O_3 and Al_2O_3-Cr_2O_3 solid solution, is formed on the surface of high-Ni alloys Fe-(20−29)Ni-(15.2–16.5)Cr-(2.3–4.3)Al at 550 °C and 600 °C in static Pb for 1000 h [22]. A long-term test duration of one year performed on Fe-14Cr-14Ni-2.5Al-1.6Mn-2.5Mo-0.9Nb steel at 550 °C in static Pb with ~10^{-7} mass%O allowed to characterize the alloy as a potential candidate for the use in lead-cooled reactors since a very thin (<100 nm) protective Al-rich oxide film was formed [23]. In the more corrosive, compared to Pb, Pb-Bi eutectic a threshold concentration for oxygen in the liquid metal was experimentally identified to be ~10^{-6} mass% at 550 °C [24]. Below this concentration the dissolution corrosion dominates over oxidation on the surface of Fe-18Ni-12Cr-2.3Al and Fe-18Ni-12Cr-2.9Al-Nb-C austenitic steels tested at 550 °C for 1000 h. Thus, in order to ensure oxidation, the necessary concentration of oxygen in the lead melts must be substantially high than that, one might expect, based on the thermodynamic stability of alumina [25], i.e. above the magnetite formation that is similar for conventional austenitic steels. It is known also that Al, similar to Cr and Mn, is highly soluble in HLM. Therefore it is important to bond these elements on the surface of the steel as an oxide layer to avoid that they will start to dissolve due to the continuous competition between dissolution and oxidation in the liquid metal system and to form oxide in the liquid metal bulk instead of the steel surface.

Today's progress in control of chemistry of Pb and Pb-Bi allows to maintain the oxygen concentrations in big volumes of flowing melt very precisely for a long period of time [15,25–27]. Surfaces of steel components facing liquid metal consume oxygen due to oxidation and therefore oxygen should be supplied continuously in order to keep the target concentration and in this way the oxidation as the dominating process in the reacting system. In case of an interruption of the oxygen supply, the oxygen concentration can drop to the dissolution corrosion domain. The latter scenario might be interpreted as unfavorable accidental conditions of operation and should be verified experimentally.

Therefore, the aim of this study is to investigate the possibility of the in-situ formation of protective oxide layers on the surface of aluminium-alloyed austenitic steels in static Pb-Bi eutectic and demonstrate the long-term durability of the formed barriers under varying oxygen concentrations in the liquid metal. The main tasks in this work are:

- To oxidize initially the steels by means of exposure to Pb-Bi eutectic with high oxidation potential, i.e. $C_{O[Pb\text{-}Bi]} > Fe_3O_4$;
- To assess the long-term durability of the formed oxide layers by means of stepwise changing oxygen concentration in the liquid metal from $C_{O[Pb\text{-}Bi]} > Fe_3O_4$ to $C_{O[Pb\text{-}Bi]} < Fe_3O_4$.

2. Materials and methods

Aluminium-alloyed austenitic Fe-14Cr-2Mn-20Ni-0.5Cu-3Al and Fe-14Cr-5Mn-12Ni-3Cu-2.5Al steels of different composition were supplied by Oak Ridge National Laboratory in annealed state (Table 1). For convenience the steels are named further in the text as high Ni and low Ni, respectively. The manufacturing procedure and mechanical properties of these steels are presented in detail elsewhere [3].

Fig. 1a and b show structure of steels obtained with the aid of scanning electron microscopy based electron back scatter diffraction (SEM-EBSD) from the areas of 895 × 665 μm on the transversal metallographic cross-sections. The pattern quality maps are overlapped with grain boundaries maps. About 700 grains were analyzed in the areas of interest. The grain size distribution, excluding twin boundaries, ranges from several microns to about 110 μm in diameter with the largest fraction between 15 and 80 μm and averages of 55 μm for both steels (Fig. 1c, d). The total length of characterized boundaries reaches about of 70 mm. The high-angle random boundaries are colored in black and coincidence site lattice (CSL) boundaries are colored in red in the Fig. 1a and b. The latter compose the largest fraction of grain boundaries of 56% and 75% for high Ni and low Ni steel, respectively. Most of the Σ3 CSL boundaries are the twin boundaries (<111 >, 60°). The Nb(Ti) carbides are detected in the composition of both steels (Fig. 1e, f). The hardness of high Ni and low Ni steel averages 307 (± 6.4) and 275 (± 16.1) HV_{500}, respectively.

For the current studies, cylindrical corrosion samples (Ø5 ×100 mm) were manufactured by means of electric discharge machining followed by final turning.

Fig. 2 shows a scheme of the experimental setup manufactured to carry out static corrosion tests. It consists of a stainless-steel autoclave with a lid. The lid provides ports for: gas inlet and outlet; thermocouple; sample holder; oxygen pump and oxygen sensor [28–30]. The autoclave contains an alumina crucible filled with 5 kg of liquid Pb-Bi eutectic. Before introducing the samples in the test setup, Pb-Bi was preconditioned with respect to temperature (500 °C) and initial oxygen concentration (10^{-6} mass%O). Both steels were exposed simultaneously in the same setup.

Fig. 3 shows the experimental parameters (temperature and oxygen concentration) recorded during the course of test. The test was performed at 500 °C for 10,000 h. The oxygen concentration in the liquid Pb-Bi was varied during the test from comparable "high" (~10^{-6} mass%

Table 1
Chemical composition of aluminium-alloyed austenitic steels.

Element mass%	High Ni steel	Low Ni steel
Fe	Balance	
Cr	13.86	14.91
Ni	19.98	12.03
Mn	2.00	4.97
Cu	0.52	3.06
Al	3.02	2.52
Si	0.12	0.11
Nb	1.01	0.59
V	0.05	0.05
Ti	0.05	0.05
Mo	1.99	0.11
W	0.96	< 0.01
C	0.148	0.201
B	0.0074	0.0097
N	0.0012	–
P	0.022	

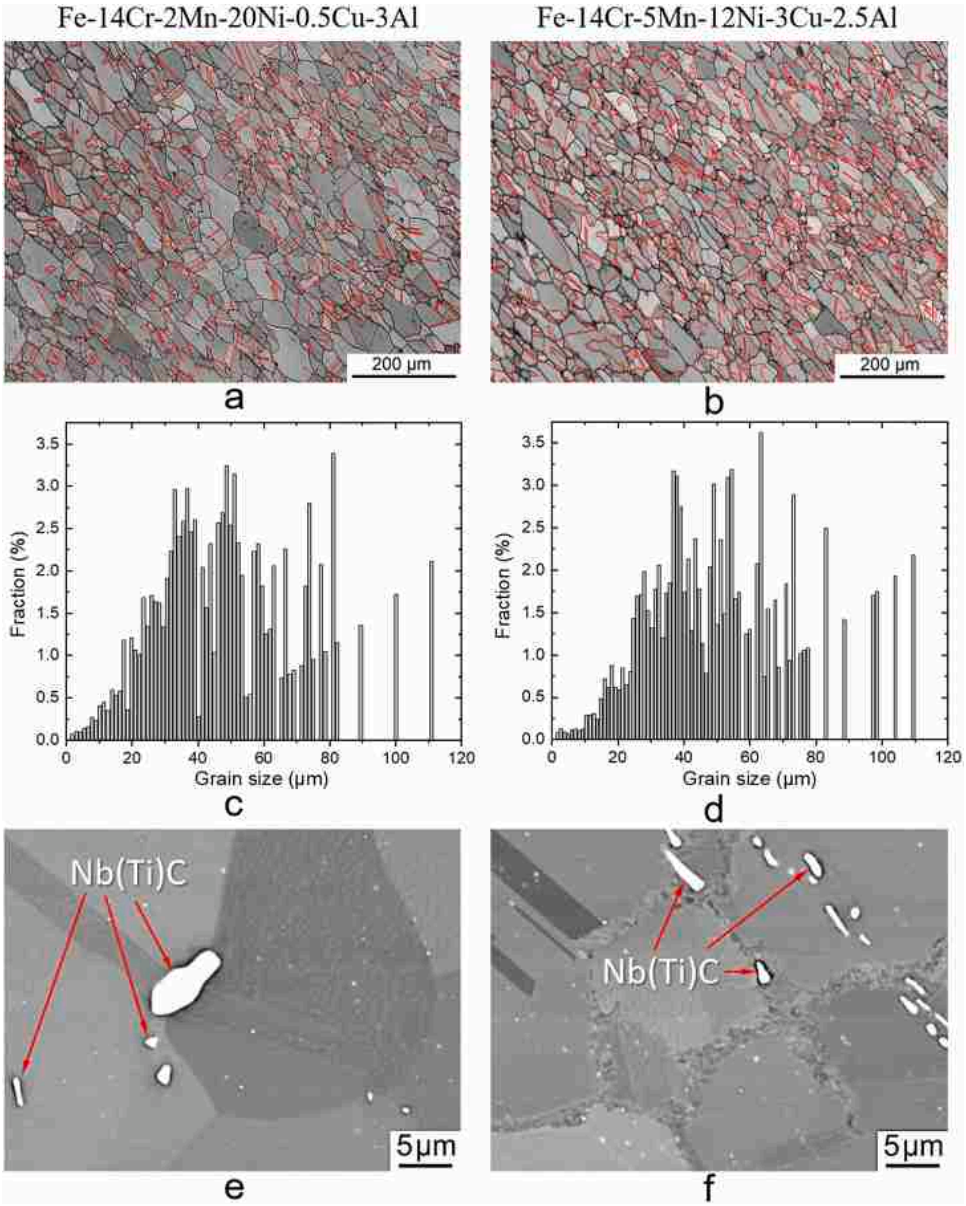

Fig. 1. Structure of Fe-14Cr-2Mn-20Ni-0.5Cu-3Al and Fe-14Cr-5Mn-12Ni-3Cu-2.5Al steels in as-received annealed state. a) and b) – EBSD pattern quality maps overlapped with grain-boundary maps with black-colored random high-angle boundaries and red-coloredwin boundaries Σ3 (<111 >, 60°). c) and d) – back-scattered electron micrographs showing precipitations of Nb(Ti)C carbides in both steels.

O) to "low" (~10^{-9} mass%O):

- 10^{-6} mass% for ~1100 h;
- ~10^{-9} mass% for ~ 700 h from 1100 to 1800 h;
- 10^{-6} mass% for ~ 3200 h from 1800 to 5200 h;
- ~10^{-9} mass% for ~ 1200 h from 5200 to 6400 h;
- 3×10^{-6} mass% for ~ 3600 h from 6400 to 10,000 h.

Dashed horizontal lines in the Fig. 3 show the concentrations of oxygen in the liquid metal which correspond to the thermodynamic equilibrium between Me/Me_xO_y (Me = Pb, Ni, Fe and Cr) for some selected oxides close to the test conditions regarding the oxygen concentration in the Pb-Bi. Thus the "high" concentration of 10^{-6} mass% O should avoid oxidation of Pb (Bi) and provide oxidation of main constituents of the alloys (Fe, Cr, Mn, Al) except Cu and Ni [25]. The "low" concentration of 10^{-9} mass% O should provide oxidation conditions for Cr, Mn and Al but not for Fe. In this way we want to determine the long-term durability of the initially formed oxide layer and the particular role of alloying elements with high affinity to oxygen, i.e., Cr, Mn and Al.

After 10,000 h exposure the samples were extracted, segmented and metallographic cross-sections (seven per one sample) were prepared. Corrosion depth was evaluated by light optical microscopy (LOM) with a routine procedure consisting of reconstruction of the initial diameter of the sample by using unaffected regions of the sample surface, detecting the center and measuring every 15° the corrosion depth relative to the reconstructed circle.

A Keyence VHX6000 digital light microscope was used for 3D microscopy, surface analysis and cross sectional metallography. A Jeol JSM6610LV scanning electron microscope (SEM) combined with a Bruker (XFLASH 4010) energy dispersive X-ray (EDX) detector was used to determine microstructure and elemental composition of corrosion zones. For high resolution microscopy the field emission SEM (FESEM) was used. X-ray photoelectron spectroscopy (XPS) was applied to analyze composition of thin oxide films.

For surface examinations, the sample segments were first cleaned

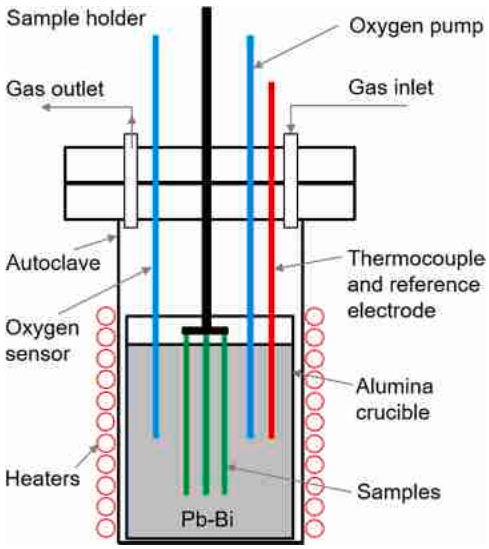

Fig. 2. Principal scheme of apparatus for corrosion tests in static Pb-Bi eutectic.

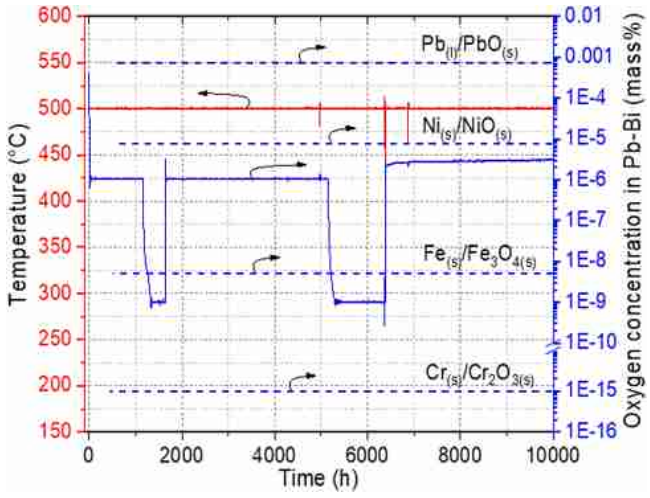

Fig. 3. Temperature and oxygen concentration in liquid Pb-Bi depending on the exposure time. Dashed lines are the concentrations of oxygen which correspond to the thermodynamic equilibrium between Me/Me_xO_y (Me = Pb, Ni, Fe and Cr).

from solidified Pb-Bi in hot glycerin at about 150 °C then degreased in ethanol followed by final chemical cleaning in a mixture of $CH_3COOH–H_2O_2–C_2H_5OH$ (1:1:1) at room temperature.

3. Results

3.1. Fe-14Cr-2Mn-20Ni-0.5Cu-3Al steel

Fig. 4 shows a general overview (a) and a more detailed (b) view of the high Ni steel sample surface after the exposure to and subsequent cleaning from Pb-Bi. The surface of the sample showed slight oxidation leading to formation of mainly golden-colored film with darker spots of presumably thicker oxide (Fig. 4b). The machining marks from samples production are still clearly visible on the surface indicating that the formed oxide is very thin.

Fig. 5 shows the XPS spectra of Fe, Cr, Ni, Al and O obtained from the surface of sample cleaned from Pb-Bi after the spattering up to the depth marked as the etch levels from # 0 to # 169 that corresponds to 0 – 2100 s of etching with a step of ~5 s. The Fe2p3 spectra revealed surface

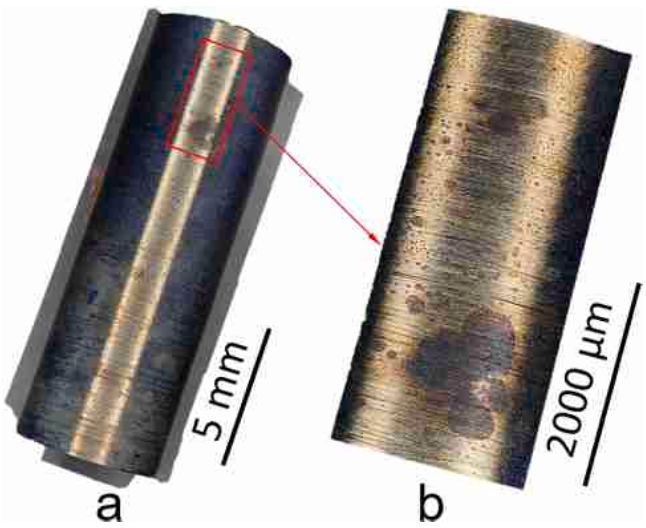

Fig. 4. Surface of the Fe-14Cr-2Mn-20Ni-0.5Cu-3Al corrosion sample after exposure at 500 °C to static Pb-Bi for 10,000 h. a) – three-dimensional overview of the corrosion sample and b) – detail out of a) with higher magnification. Sample is cleaned chemically with respect to solidified Pb-Bi.

peaks within the etching levels ranging from #0 to # 35 with a binding energy of 710.5 eV which corresponds to the oxidation state of Fe and might be associated with $Fe_xCr_{3-x}O_4$ spinel (Fig. 5a) [31,32]. In the deeper regions (etch levels # 36 – 169), the peaks of metallic Fe at 706.8 eV are observed. The peaks of Cr2p at 577.2 eV are consistent with the mixed chromium oxide detected from the surface up to the etching level # 50, which is a bit deeper than that one of Fe oxide. With a depth the peaks of metallic Cr at 574.3 eV are appeared (Fig. 5b) [32]. The only peaks of metallic Ni are detected with binding energy of 852.8 eV starting from the etching level # 37 (Fig. 5c). The weak signals corresponding to the Al oxide at 76.0 eV are detected at the surface and reaching maximum at the etch level # 45 followed by gradual decreasing in signal counts up to the level # 80 after which the weak signals of metallic Al at 72.8 eV are detected (Fig. 5d). The oxygen 1 s spectra are detected up to the etch level # 70 clearly revealing the ranges of the oxide film (Fig. 5e). The very first peak of oxygen observed at the level # 0 and binding energy of 533.8 eV correlates with the water organic oxygen contaminating surface of sample and disappearing after the first sputtering cleaning [31]. The O1s spectra binding energies change with etching depth from 530.7 eV (# 1) to 530.9 eV (#2–21) and further to 531.2 eV (# 30) and 532.0 eV (# 50). The metal oxides are detected usually at the binding energies of 529–530 eV [31]. Alumina has a O1s signal at 531.1 eV which agrees with our data. The binding energies at 531–533 eV are usually associated with hydroxyls which should not be the our case, especially for the deeper levels of etching. Therefore the high energy peaks detected in O1s spectra should be attributed to the defected spinel [31,33].

The depth profiles of elements in the oxide and sub-oxide zone are shown in Fig. 6. Based on the profile and the XP spectra (Fig. 5) the oxide film is composed of Cr(Fe) and Al. It has a bilayer structure with Cr(Fe)-rich oxide film at the top and intermediate Al-rich oxide layer. Nickel does not present in the oxide layers.

During the general examination of the sample surface, cleaned with respect to solidified Pb-Bi, the areas which might be interpreted as dissolution corrosion were not detected. However the very detailed examination of the complete sample surface allow us to reveal the presence of the very rare pit-type corrosion damages (Fig. 7). The typical pit-type damage consists of the central spot and a circular lacy-like cover with the diameters ranging from about 65 to 150 µm and averaging ~108 (± 30) µm. In some cases the pit center looks as a hole of several microns in the depth and in the diameter (Fig. 8). In another cases the pit

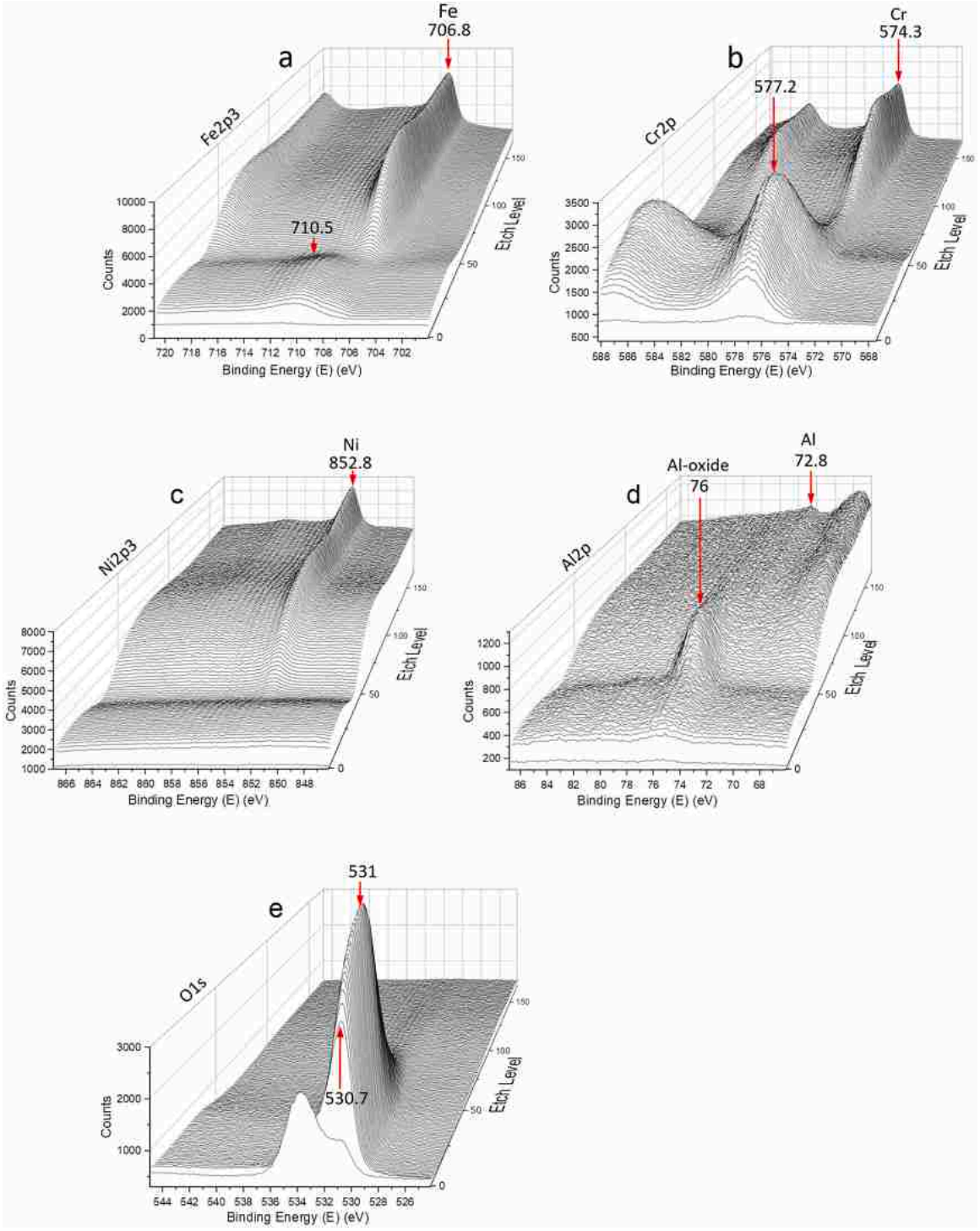

Fig. 5. XPS spectra as function of depth obtained from the surface of Fe-14Cr-2Mn-20Ni-0.5Cu-3Al steel exposed at 500 °C to static Pb-Bi eutectic for 10,000 h. a) Fe2p3; b) Cr2p; c) Ni2p3; d) Al2p and e) O1s.

center is covered by the faceted oxide crystallites composed of Fe and Mn (Fig. 9a, b, A) while the area around the pit center is covered by the more complex oxide film composed of Cr, Fe, Al and Mn (Fig. 9b, B). In the most of the observations, the center of the pit is placed directly on the turning mark indicating in favor of interconnection between the surface machining, which introduces defects in the near-surface zone, and a subsequent corrosion response of the damaged surface areas (Figs. 7, 8a). The lacy cover is a spongy-like corroded surface depleted markedly in Mn and Ni, enriched in Cr and Al and percolated by Pb and Bi, in spite of the performed cleaning (Fig. 9c, C). The area near by the lacy cover, which at first sight looks undamaged, is however also depleted in Mn and Ni although is still yet covered by the thin Al- rich oxide film (Fig. 9c, D). Formation of the pit-type corrosion damages with the lacy covers is well known from the electrochemical corrosion [34, 35]. Although, the electro-chemical processes does not take place in the liquid metals, the very similar shape of the localized corrosion damages might indicate about possible phenomenological similarities in the mechanisms of formation which, in the case of the liquid metal, is the dissolution-driven process resulting in selective leaching of steel constituents [7].

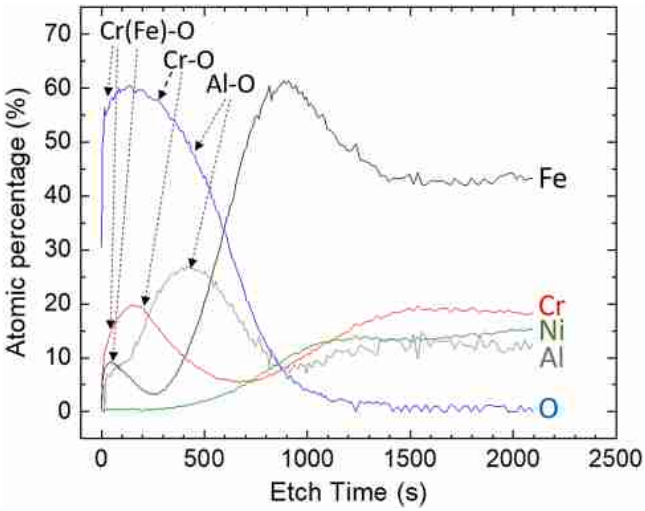

Fig. 6. XPS depth profiles of elements in oxide and sub-oxide layers formed on the surface of Fe-14Cr-2Mn-20Ni-0.5Cu-3Al steel after test at 500 °C in static Pb-Bi eutectic for 10,000 h.

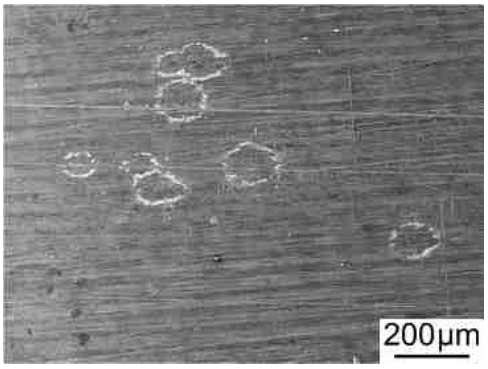

Fig. 7. Secondary-electron image of surface area populated with pits on Fe-14Cr-2Mn-20Ni-0.5Cu-3Al sample after the test at 500 °C in static Pb-Bi eutectic for 10,000 h. Sample is cleaned chemically with respect to solidified Pb-Bi.

Several pits with lacy covers were milled from the surface by means of focused ion beam approximately in the middle in order to investigate the details of near-surface structure and composition of the pit on the micro cross-section. Fig. 10 a shows characteristic back-scattered electron image of the pit cross-section. The pit center is a hemispherical oxide intrusion formed on the basis of steel matrix (Fig. 10 b). The very thin oxide film covers irregularly the surface in the vicinity of the pit center (Fig. 10 b) and interrupted on the surface of lacy cover (Fig. 10 c, d). The near-surface structure of pit differs substantially from the annealed steel matrix (Fig. 1a). It consists of about 5 μm thick fine-grained zone adjoining surface followed by the intermediate zone with deformation bands (Fig. 10 b-d). The fine-grained zone is percolated by Pb-Bi revealed in the view of white spots on the light-gray background of fine grains. It is interesting to note that liquid metal does not percolate further into the deformed zone, at least at this stage of the pit development.

The structurally-modified near-surface zone, consisted of the fine-grained (3.4 (± 2.0) μm) and deformed (20–25 μm) zones, is not related only to the pit-type damages but also observed continuously along the complete circumference of the cross-sections prepared in the standard metallographic way. Thus Fig. 11 a shows the typical morphology of the corrosion-intact near-surface zone which clearly shows both mentioned structures. The EDX line profile of main elements of steel across the near surface zone indicates about a noticeable redistribution of Fe, Cr, Ni and Mn within the 3–5 μm thick fine-grained part of the structurally-modified zone (Fig. 11 b). The hardness of the near-surface zone is markedly higher (408 (± 37.6) HV_{50}) in comparison with the annealed steel bulk (345 (± 9.6) HV_{50}).

The formation of the structurally-modified near-surface zone is attributed to the preparation stage of cylindrical samples, namely to the final turning step. It is believed that the formation of the fine-grained part of this zone is deformation-induced, i.e. not caused by recrystallization processes [36]. The possible effect of this zone on the corrosion response of steels is discussed in the paragraph 4.

Regular cross-section examinations showed that the high Ni steel remained in general corrosion-intact. This result does not contradict to the surface observations when the pit-type corrosion damages were revealed (Fig. 7), since it is difficult to cross the damages which are unevenly and rarely observed over the sample surface during the standard preparation of metallographic cross-sections. This result however underlines the importance of comprehensive examination of both surface and cross-sections in order to reveal the complete and realistic picture of the corrosion interaction.

The high resolution SEM images of the near-surface zone are shown in Fig. 12. The surface of steel is covered by a continuous and very thin oxide film (Fig. 12 a). The oxide film has a bilayer structure with a thickness of about 200 nm in the average (Fig. 12 b). Based on the EDS analysis carried out along the oxide cross-section, the outer sub-layer is a Cr-based oxide (Fig. 13). The inner sub-layer is enriched in Al. In the sub-oxide zone the Cr-depleted layer is detected confirming diffusion of Cr toward surface to form outer Cr-rich oxide layer. After the Cr-depleted layer the zone with serrated increased chromium content is detected followed by the secondary Cr-depleted zone after which the

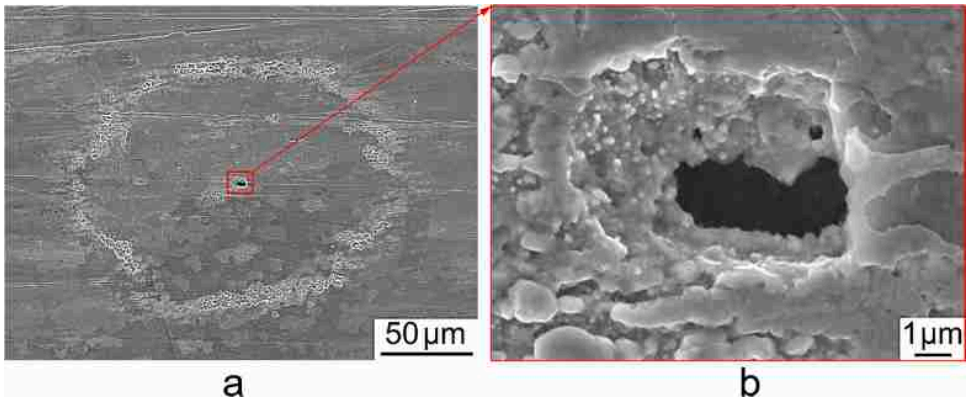

Fig. 8. Secondary-electron images of separated pit formed on the surface of Fe-14Cr-2Mn-20Ni-0.5Cu-3Al sample after the test at 500 °C in static Pb-Bi eutectic for 10,000 h. Sample is cleaned chemically with respect to solidified Pb-Bi.

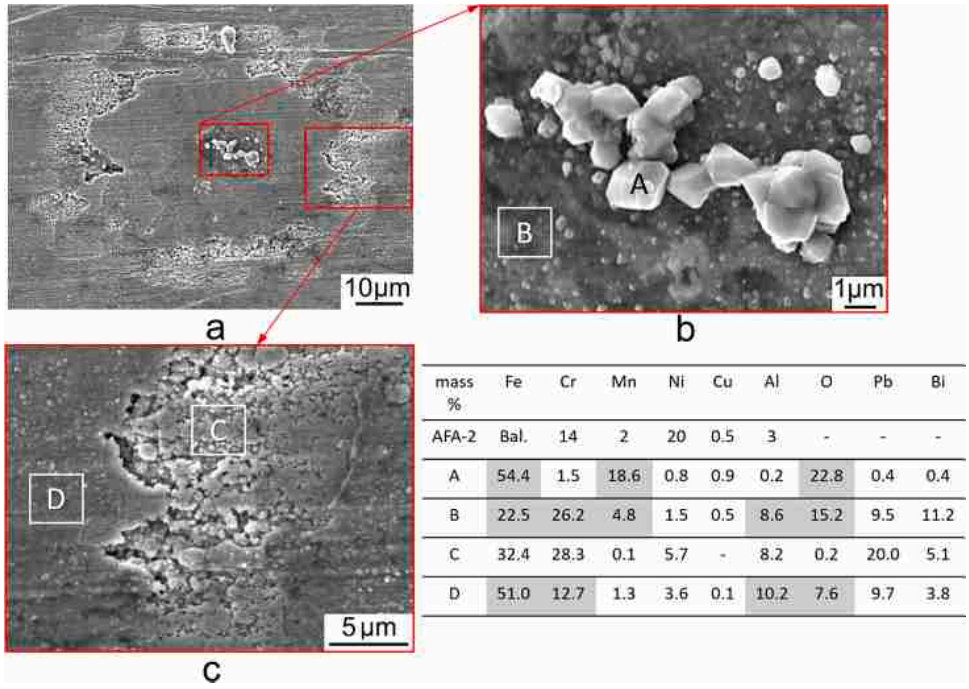

mass %	Fe	Cr	Mn	Ni	Cu	Al	O	Pb	Bi
AFA-2	Bal.	14	2	20	0.5	3	-	-	-
A	54.4	1.5	18.6	0.8	0.9	0.2	22.8	0.4	0.4
B	22.5	26.2	4.8	1.5	0.5	8.6	15.2	9.5	11.2
C	32.4	28.3	0.1	5.7	-	8.2	0.2	20.0	5.1
D	51.0	12.7	1.3	3.6	0.1	10.2	7.6	9.7	3.8

Fig. 9. Secondary-electron images of separated pit formed on the surface of Fe-14Cr-2Mn-20Ni-0.5Cu-3Al sample after the test at 500 °C in static Pb-Bi eutectic for 10,000 h. Sample is cleaned chemically with respect to solidified Pb-Bi.

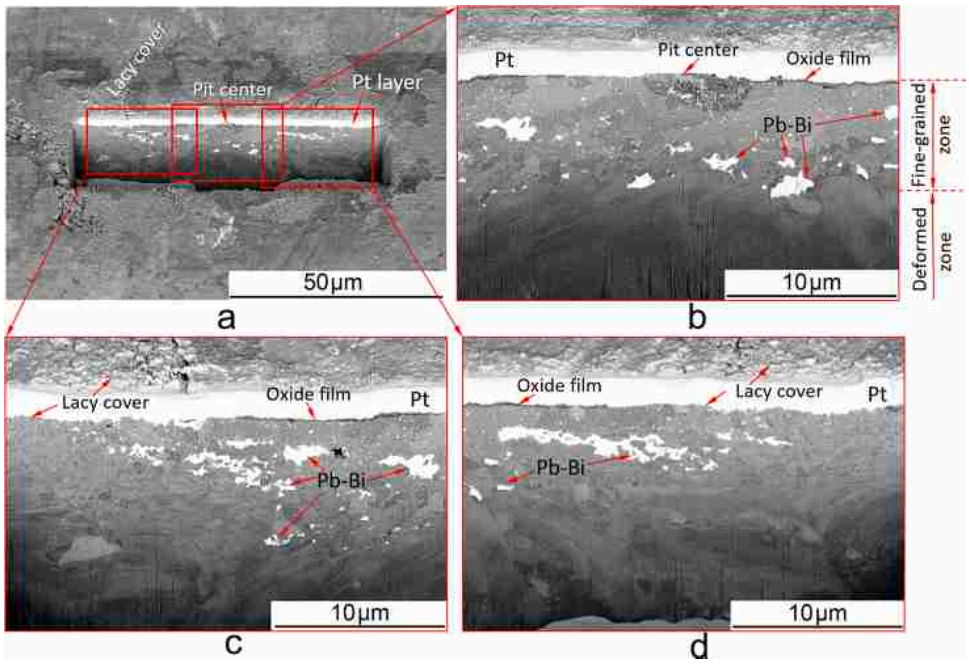

Fig. 10. Back-scattered electron images of pit cross-section, made by surface milling with focused ion beam. Surface of Fe-14Cr-2Mn-20Ni-0.5Cu-3Al sample after the test at 500 °C in static Pb-Bi eutectic for 10,000 h. Sample is cleaned chemically with respect to solidified Pb-Bi.

chromium content stabilizes at level corresponding to the steel composition (Fig. 13). One might reasonably assume that the sub-oxide zone with marked redistribution of elements detected in the range of 500–2100 nm on the X axis (Fig. 13) correlates with the fine-grained part of the structurally-modified zone (Fig. 11).

The distribution of elements measured by EDS line analysis agrees very well with the XPS profile obtained through the depth of oxide film starting from surface (compare Figs. 6 and 13) and confirms the bilayer structure (Cr/Al) of the formed oxide film.

3.3. *Fe–14Cr–5Mn–12Ni–3Cu–2.5Al steel*

Fig. 14 shows a general overview (a) and more detailed view (b) of the surface of the low Ni steel sample after exposure to and subsequent removal from the solidified Pb-Bi. Similar to the high Ni steel the slight surface oxidation is observed (Fig. 14 b).

The characteristic XP spectra of Fe, Cr, Ni, Mn, Al and O obtained through the depth of oxide film from the surface of cleaned sample are shown in Fig. 15. The Fe2p3 spectra, within the surface etch levels

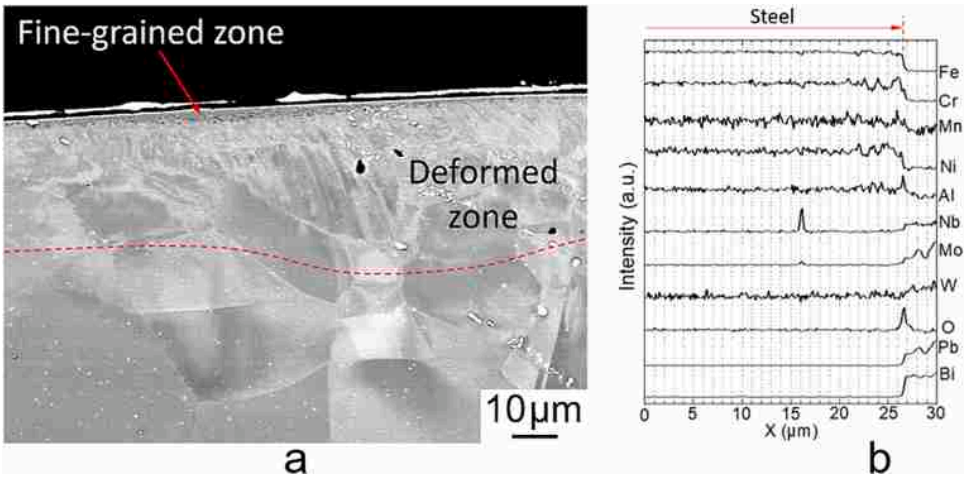

Fig. 11. Morphology and composition of near-surface zones observed on the transversal cross-sections of cylindrical sample of Fe-14Cr-2Mn-20Ni-0.5Cu-3Al steel after the test at 500 °C in static Pb-Bi eutectic for 10,000 h. a) - back-scattered electron image; b) - profiles of elements in the structurally-modified near-surface zone of steel.

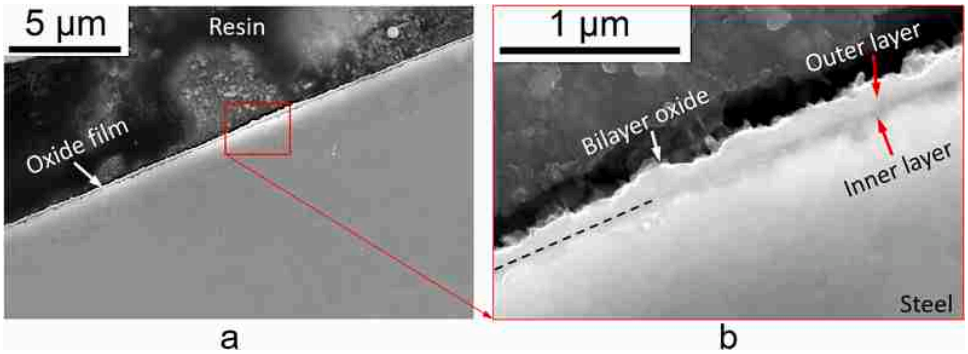

Fig. 12. Cross section of the Fe-14Cr-2Mn-20Ni-0.5Cu-3Al steel sample after test at 500 °C in static Pb-Bi eutectic for 10,000 h. a) – general view of surface and near-surface zones. b) – detailed view of oxide layer and sub-oxide zone specified by area in a).

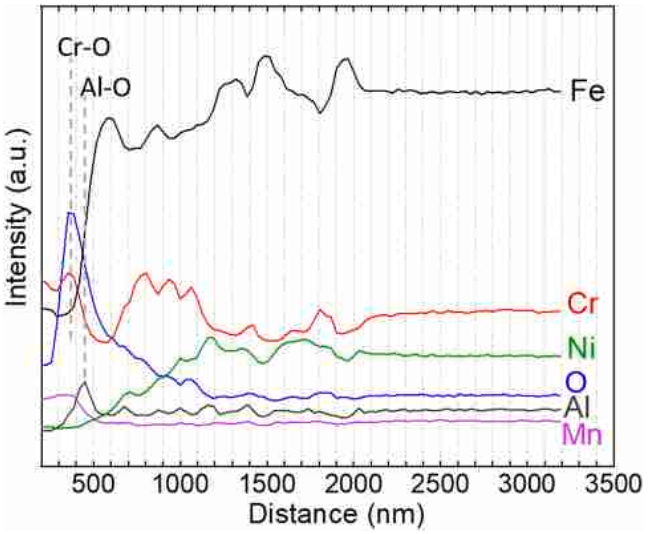

Fig. 13. Distribution of elements in oxide and sub-oxide layers formed on the surface of Fe-14Cr-2Mn-20Ni-0.5Cu-3Al steel sample after test at 500 °C in static Pb-Bi eutectic for 10,000 h.

ranging from # 0 to # 19 show peaks with the binding energies of 710.5 eV corresponding to the oxidation state of Fe that might be associated with $Fe_xCr_{3-x}O_4$ spinel (Fig. 15 a) [31]. The metallic Fe with

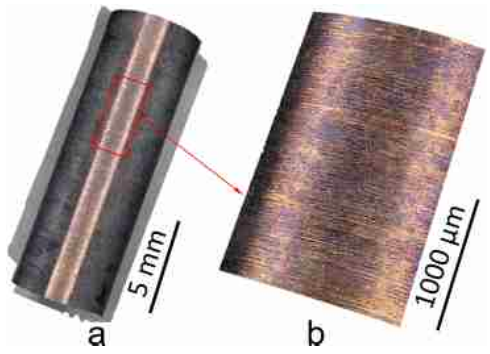

Fig. 14. Surface of the Fe-14Cr-5Mn-12Ni-3Cu-2.5Al corrosion sample after exposure at 500 °C to static Pb-Bi for 10,000 h. a) – three-dimensional overview of the corrosion sample and b) – detail out of a) with higher magnification. Sample is cleaned chemically with respect to solidified Pb-Bi.

707.1 eV is detected in the deeper regions (etch levels # 23-104). The peaks of Cr2p at 577.3 eV are consistent with the chromium oxide detected up to the etching level # 30 (Fig. 15 b) [32]. The peaks of metallic Cr at 574.3 eV are revealed in the range of the etching levels # 30–104 (Fig. 15 b). Metallic Ni at 853.0 eV is detected within the etching levels # 24–104 (Fig. 15 c). The Mn2p spectra at the surface levels # 1 – 40 correspond to the Mn-oxide with binding energy of 642 eV (Fig. 15 d) [32]. The oxidizing state of Mn is detected up to the last etch level # 104

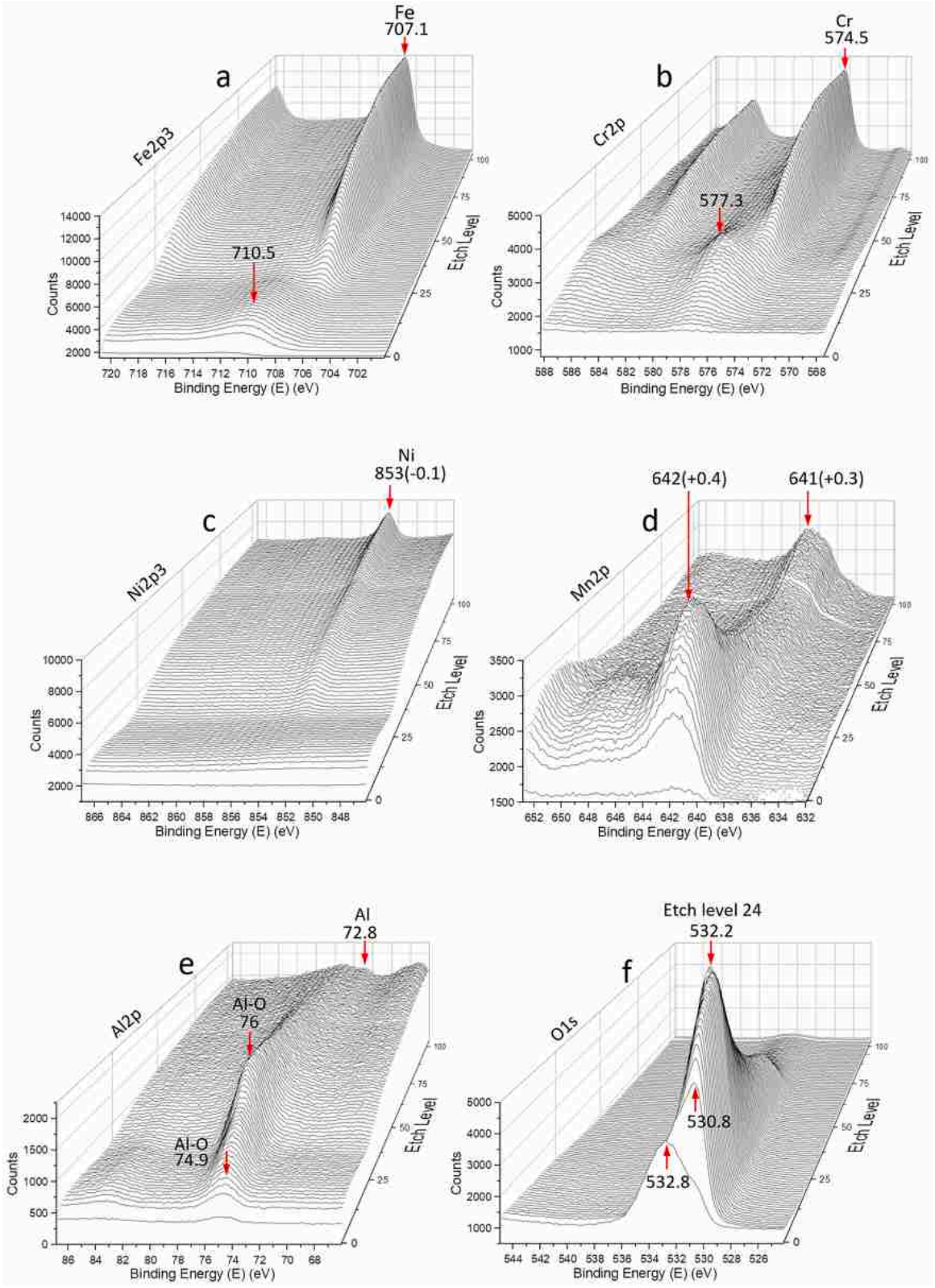

Fig. 15. XPS spectra as function of depth obtained from the surface of Fe-14Cr-5Mn-12Ni-3Cu-2.5Al steel exposed at 500 °C to static Pb-Bi eutectic for 10,000 h. a) Fe2p3; b) Cr2p; c) Ni2p3; d) Mn2p; e) Al2p and f) O1s.

with decrease in the binding energy to 641 (+0.3) eV. The Al2p signals corresponding to the Al oxide change at the surface layer from 74.9 to 76 eV at etch level # 30 and continued to be detected at the deeper etching levels (Fig. 15 e). The weak signals of metallic Al at 72.8 eV are detected starting from the etch level # 95. The strong O1s spectra are detected up to the etch level # 75 clearly revealing the ranges of the oxide film (Fig. 15 f). Similar to the XP spectra obtained from the high Ni-steel (Fig. 5e) the binding energies of O1s signals change with the

etching depth from 530.7 eV (# 1–12) to 531.5 eV (# 18) and further to 532.2 eV (# 24) and 532.7 eV (# 48) that most probably indicates about formation of defected oxides [31,33].

Fig. 16 shows the depth profiles of elements in the oxide and sub-oxide zone. Interpretation of the peaks (Fig. 15) and profiles (Fig. 16) results in the assignment of the surface oxide film with a Al-based oxide slightly alloyed at the surface by Fe, Mn and Cr.

Detailed surface examination of exposed and cleaned sample reveals a parallel-arranged vermicular nodules oriented perpendicular with respect to the main longitudinal axis of the sample (marked by arrows in Fig. 17 a). The length of these nodules is in the order of several tens of microns, while the width and the height are in the order of several microns (see Fig. 17 b). The nodule consists of an agglomerate of faceted oxide crystallites which according to the EDX analysis contain mainly Fe (~50 mass%) and Mn (~20 mass%) (Fig. 17 c). The formation of these vermicular protrusions might be correlated to surface pattern stemming from the final turning step of sample manufacturing. One might speculate that these places are prone to a more intensive oxidation due to the formation of thicker oxide protrusions. Re-precipitation of initially leached components can be excluded since it should have a more random character and would not be associated with the surface pattern.

Fig. 18 a shows the typical morphology of the near-surface zone observed on the metallographic cross-sections of low Ni steel. Similar to the high Ni steel, two distinct zones are observed. The top surface zone with the fine-grained structure is however about three times thicker and reaches of 15.9 (± 3.3) μm in depth. It looks rooted into the steel bulk. The redistribution of Fe, Cr, Mn, Ni and Cu is detected within this zone (Fig. 18 b). The near-surface zone characterized by increased surface hardness reached of 363 (± 6.8) HV_{50} while the hardness of annealed matrix averaged 304 (± 15) HV_{50}.

High-resolution micrographs, obtained from the sub-oxide zone, allow to reveal that the grain size even decreases towards the oxide film from the fine-grains with average grain size of about 1 μm to the ultra-fine grains with the grain size of 300 (± 100) nm (Fig. 19 a). A continuous monolayer of oxide film with a thickness averaging 50 nm is revealed (Fig. 19 b).

The depth profiles of elements in the oxide and sub-oxide zone are shown in Fig. 20. Based on the profile and the XP spectra (Fig. 15) the oxide film is composed mostly of Al and slightly alloyed by Fe and Mn with Cr enrichment beneath. Nickel does not present in the oxide layer.

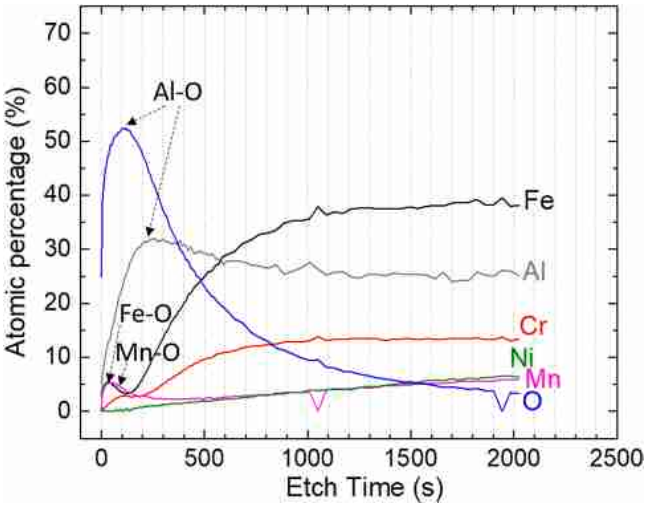

Fig. 16. XPS depth profiles of elements in oxide and sub-oxide layers formed on the surface Fe-14Cr-5Mn-12Ni-3Cu-2.5Al steel after test at 500 °C in static Pb-Bi eutectic for 10,000 h.

4. Discussion

The experimental data presented above show that Al-alloyed austenitic steels with “high” and “low” Ni content demonstrated in general a very good long-term (10,000 h) corrosion resistance in static Pb-Bi eutectic at 500 °C under the variation in corrosion conditions of test from oxidizing to dissolving liquid metal (Fig. 3). Steels were demonstrated mostly slight oxidation which is a very promising result for their qualification as a candidate material for the application in contact with the Pb-based melts (Pb, Pb-Bi).

The low Ni steel does not show the corrosion damages which might be associated with the localized leaching of steel constituents by liquid metal. In the case of high Ni steel, however, the rare pits were detected on the surface indicating about the initiation of the dissolution corrosion. This, most probably, is a result of different oxidation behavior between the steels. Thus, the oxidation of the high Ni steel resulted in the formation of the bilayer oxide film with the outer Cr(Fe)-based and inner Al-rich oxide sub-layers of 200 nm thickness on average. The four times thinner (50 nm) single layer of Al-rich oxide was formed instead on the surface of low Ni steel. The Al-based oxide film therefore might be characterized as a more protective. In this view the low Ni steel alloyed by Al indeed might be called as an alumina-forming austenitic steel (AFA) similar to the widely used name of this class of steels and alloys developed specifically for the high-temperature application in gaseous environments.

The oxide films formed on the surface of both steels showed in general good durability under the purposeful and controlled repetitive changes in the oxygen concentration in the liquid metal in order to provide oxidation and dissolution corrosion modes. One might suppose that the steels form oxide films during the initial period (~1100 h) when liquid Pb-Bi eutectic has high oxidation potential (10^{-6} mass%). As the concentration of oxygen decreased to ~10^{-9} mass%, in order to provide dissolving conditions of the liquid metal, the initially formed oxide film might start to degrade locally. A decrease in the oxygen concentration should destabilize the Fe-based oxides since 10^{-9} mass% O is already below the stability of magnetite (Fe_3O_4) at 500 °C [25]. However the oxides formed on the steels are composed of the elements that have higher affinity to oxygen than Fe, i.e. of Cr and Al and therefore continuing act as an effective protective barriers against the dissolution corrosion. After the following return to the oxidizing conditions of the Pb-Bi, these oxide films are already operating as an oxidation-resistant barriers. The re-healing processes, of potentially degraded surface areas of oxide, might also take place after the return to the oxidizing melt. With further cycles, the corrosion interaction should not differ substantially. However, as it was discussed above, the localized dissolution corrosion is observed after 10,000 exposure on high Ni steel covered by bilayer Cr/Al oxide film. There are a lot of potentially possible reasons which might explain the initiation of the pit-type damages as a result of degradation in protective properties of first formed oxide layer by means of the speculations around the local compositional inhomogenities arising from the side of the liquid as-well as solid metals. However here we would like to focus on the possible role of the clearly observable structural feature of steels namely on the effect of near-surface zone with modified structure formed as a result of surface machining.

As it was shown in the results, the structurally-modified zone consists of a fine-grained sub-zone at the top and an intermediate deformed sub-zone followed by the “normal” annealed structure of steel. The fine-grained zone is about five times thicker for low Ni steel (compare Fig. 11 a and Fig. 18 a). This might be a possible logical reason of marked compositional differences in oxide films formed on the steels. The presence of a structurally-modified near-surface zone might affect the corrosion response of the steels in different manner depending on the dominating corrosion mode, i.e. oxidation or dissolution. In the latter case, the fine-grained and deformed structure of the near-surface zone should only accelerate the dissolution attack. In contrast, in the

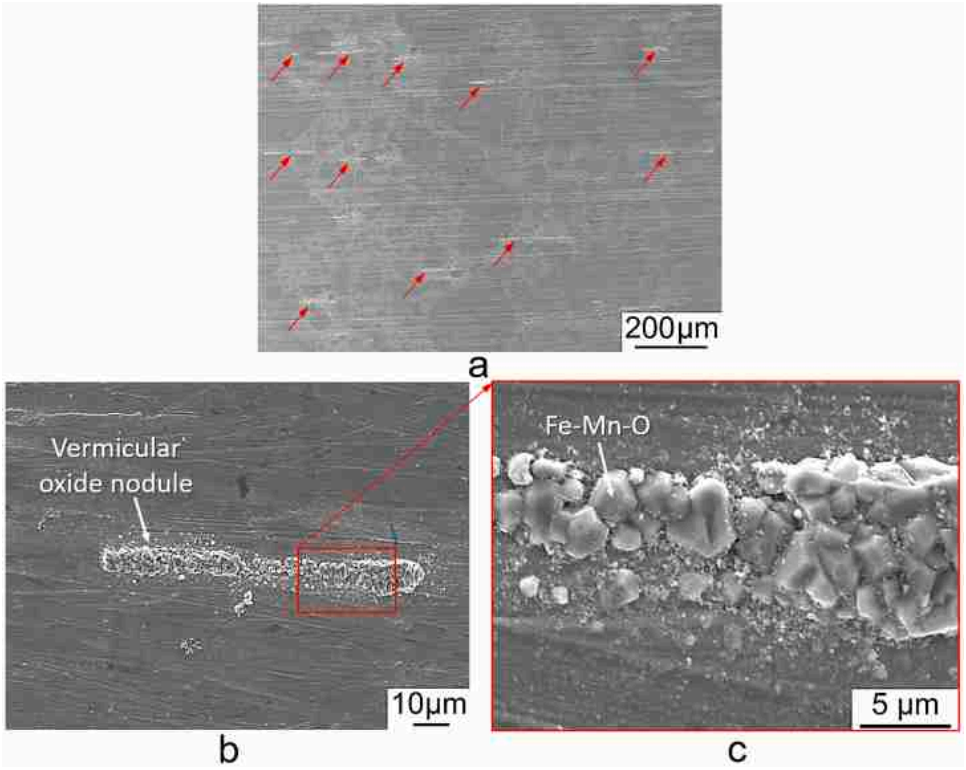

Fig. 17. Morphology of surface of Fe-14Cr-5Mn-12Ni-3Cu-2.5Al sample after the test at 500 °C in static Pb-Bi eutectic for 10,000 h. Sample is cleaned chemically with respect to solidified Pb-Bi.

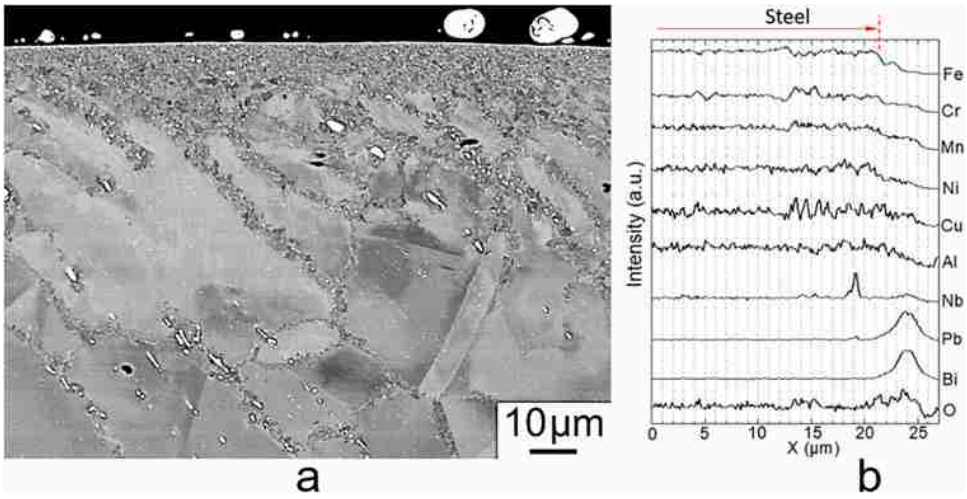

Fig. 18. Morphology and composition of near-surface zones observed on the transversal cross-sections of cylindrical sample of Fe-14Cr-5Mn-12Ni-3Cu-2.5Al steel after the test at 500 °C in static Pb-Bi eutectic for 10,000 h. a) - back-scattered electron image; b) - profiles of elements in the structurally-modified near-surface zone of steel.

oxidizing liquid metal, the near-surface zone might provide the formation of a more protective oxide layer due to the structurally-enhanced diffusion of Cr and Al into oxide layers, that is well known from the gaseous oxidation [37]. Accordingly, the corrosion response of steels is always a combined action of alloying and structure from the side of the solid metal and chemistry of the liquid metal. The favorable combination of these factors may result in formation of protective oxide barriers similar to those we are observing in this work. The unfavorable combination of these factors, like alloying by highly soluble elements, high density of structural borders and conditions in the liquid metal promoting leaching of steel constituents, will only favor the initiation and development of the dissolution corrosion.

The results obtained in this work corroborate very well with the our previous findings regarding effect of bulk structure and surface finish on the corrosion response of steels to lead-based liquid metals, i.e.: structural factors which, on the one hand, favor oxidation, might, on the other hand, promote the dissolution attack [16, 38–42]. However, in this work, we were able to study in more detail the structure and composition features of the near-surface zones formed by turning. The obtained results agreed very well with the effect of machining-induced near--surface structural transformations on steels which contact other than liquid metals corrosion media [43–46].

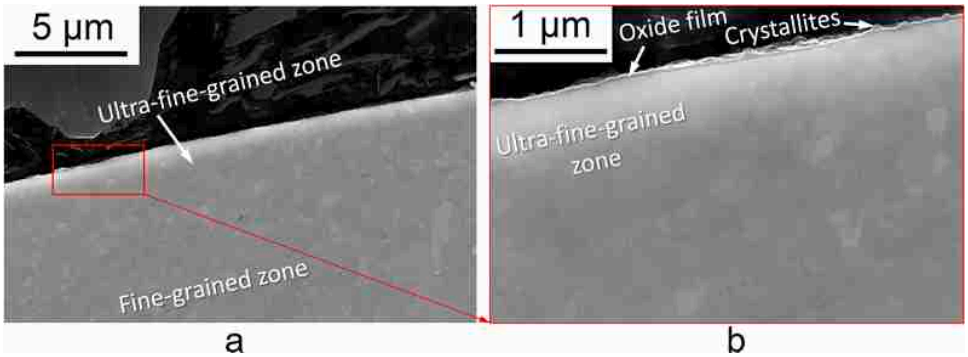

Fig. 19. Structure of oxide film and sub-oxide zone formed on the surface of Fe-14Cr-5Mn-12Ni-3Cu-2.5Al steel after test at 500 °C in static Pb-Bi eutectic for 10,000 h.

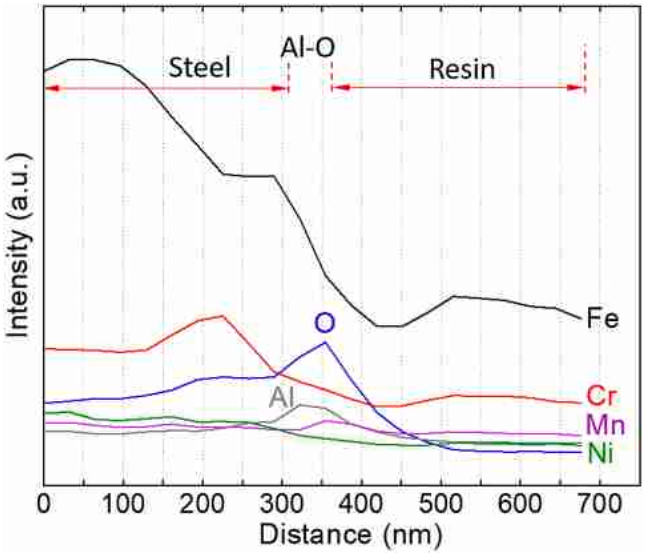

Fig. 20. Distribution of elements in oxide and sub-oxide layers formed on the surface of Fe-14Cr-5Mn-12Ni-3Cu-2.5Al steel sample after test at 500 °C in static Pb-Bi eutectic for 10,000 h.

5. Conclusions

A long-term corrosion test for a duration of 10,000 h was carried out to characterize the corrosion performance of aluminium-alloyed Fe-14Cr-2Mn-20Ni-0.5Cu-3Al and Fe-14Cr-5Mn-12Ni-3Cu-2.5Al austenitic steels at 500 °C in a static Pb-Bi eutectic depending on the concentration of dissolved oxygen which varied during the course of test from "high" (~10^{-6} mass%) to "low" (~10^{-9} mass%) providing domination of oxidation and dissolution interaction modes between steels and liquid metal, respectively. The experimental results allow the following conclusions to be formulated:

- Fe-14Cr-2Mn-20Ni-0.5Cu-3Al and Fe-14Cr-5Mn-12Ni-3Cu-2.5Al steels formed very thin and protective bilayer Cr(Fe)-O/Al-O (~200 nm) and single layer Al(Mn, Fe, Cr)-O (~50 nm) oxide films, respectively;
- Formed oxide films showed high durability during the repeating change of the corrosion character of liquid Pb-Bi from the oxidizing into the dissolving medium;
- Rare corrosion pits revealed on the high Ni steel indicate that formed Cr(Fe)-O/Al-O oxide film might fail locally the protective properties resulting in initiation of localized dissolution corrosion;
- Both steels are characterized here as a potential candidate materials for application in Pb-Bi eutectic.

CRediT authorship contribution statement

Valentyn Tsisar: Conceptualization, Methodology, Validation, Investigation, Resources, Data Curation, Writing - Original Draft, Writing - Review & Editing, Supervision. **Erich Stergar:** Conceptualization, Resources, Writing - Review & Editing, Supervision, Project administration, Funding acquisition. **Serguei Gavrilov:** Conceptualization, Methodology, Validation, Investigation, Resources, Data Curation, Writing - Review & Editing, Supervision, Project administration. **Wouter Van Renterghem:** Formal analysis, Writing - Review & Editing. **Pierre Louette:** Formal analysis, Visualization. **Stéphane Lucas:** Formal analysis, Visualization.

Declaration of Competing Interest

The authors declare that they have no known competing financial interests or personal relationships that could have appeared to influence the work reported in this paper.

Data availability

The raw/processed data required to reproduce these findings cannot be shared at this time as the data also forms part of an ongoing study.

Acknowledgments

The investigations performed in the framework of the ongoing program of characterization of compatibility of candidate materials with liquid Pb-Bi eutectic for development of the MYRRHA irradiation facility. The research leading to these results is partially funded by the European Commission HORIZON 2020 Framework Programme under grant agreement No. 755269. The authors are very thankful to Mr. Michael P. Brady (Materials Science and Technology Division, Oak Ridge National Lab, Oak Ridge, TN 37831-6115, USA) for supplying AFA steels. The authors would like to thank for the technical support to Mr. Joris Jasper and Mr. Yves Florenty and for assistance in FESEM to Ms. Lopes Maia Eloa (SCK.CEN).

References

[1] M.P. Brady, Y. Yamamoto, M.L. Santella, P.J. Maziasz, B.A. Pint, C.T. Liu, Z.P. Lu, H. Bei, The development of alumina-forming austenitic stainless steels for high-temperature structural use, JOM 60 (2008) 12–18, https://doi.org/10.1007/s11837-008-0083-2.
[2] Y. Yamamoto, M.P. Brady, M.L. Santella, H. Bei, P.J. Maziasz, B.A. Pint, Overview of strategies for high-temperature creep and oxidation resistance of alumina-forming austenitic stainless steels, Met. Mat. Trans. A 42 (2011) 922–931, https://doi.org/10.1007/s11661-010-0295-2.
[3] M.P. Brady, J. Magee, Y. Yamamoto, D. Helmick, L. Wang, Co-optimization of wrought alumina-forming austenitic stainless steel composition ranges for high-temperature creep and oxidation/corrosion resistance, Mater. Sci. Eng. A 590 (2014) 101–115, https://doi.org/10.1016/j.msea.2013.10.014.

[4] M.P. Brady, G. Muralidharan, Y. Yamamoto, B.A. Pint, Development of 1100 °C Capable Alumina-Forming Austenitic Alloys, Oxid. Met (2016), https://doi.org/10.1007/s11085-016-9667-3.

[5] I.G. Dmukhovskaya, V.V. Popovich, A phenomenological model of embrittlement of metals under conditions of the adsorption action of liquid metal media, Sov. Mater. Sci. a Transl. Fiz. khimicheskaya mekhanika Mater./Acad. Sci. Ukr. SSR 18 (1983) 461–467, https://doi.org/10.1007/BF00729424.

[6] OECD-NEA, Handbook on lead-bismuth eutectic alloy and lead properties, materials compatibility, thermal-hydraulics and technologies, OECD Twent. (2015).

[7] C. Schroer, O. Wedemeyer, J. Novotny, A. Skrypnik, J. Konys, Selective leaching of nickel and chromium from Type 316 austenitic steel in oxygen-containing lead–bismuth eutectic (LBE), Corros. Sci. 84 (2014) 113–124, https://doi.org/10.1016/j.corsci.2014.03.016.

[8] B.A. Shmatko, A.E. Rusanov, Oxide protection of materials in melts of lead and Bismuth, Mater. Sci. 36 (2000) 689–700.

[9] I.V. Gorynin, G.P. Karzov, V.G. Markov, V.A. Yakovlev, Structural materials for atomic reactors with liquid metal heat-transfer agents in the form of lead or lead—bismuth alloy, Met Sci. Heat. Treat. 41 (1999) 384–388, https://doi.org/10.1007/BF02469876.

[10] O. Yeliseyeva, V. Tsisar, G. Benamati, Influence of temperature on the interaction mode of T91 and AISI 316L steels with Pb–Bi melt saturated by oxygen, Corros. Sci. 50 (2008) 1672–1683, https://doi.org/10.1016/j.corsci.2008.02.006.

[11] P. Hosemann, R. Dickerson, P. Dickerson, N. Li, S.A. Maloy, Transmission electron microscopy (TEM) on oxide layers formed on D9 stainless steel in lead bismuth eutectic (LBE), Corros. Sci. 66 (2013) 196–202, https://doi.org/10.1016/j.corsci.2012.09.019.

[12] E. Charalampopoulou, R. Delville, M. Verwerft, K. Lambrinou, D. Schryvers, Transmission electron microscopy study of complex oxide scales on DIN 1.4970 steel exposed to liquid Pb–Bi eutectic, Corros. Sci. 147 (2019) 22–31, https://doi.org/10.1016/j.corsci.2018.10.018.

[13] C. Schroer, J. Konys, Quantification of the Long-Term Performance of Steels T91 and 316L in Oxygen-Containing Flowing Lead-Bismuth Eutectic at 550 °C, J. Eng. Gas. Turbines Power 132 (2010) 82901, https://doi.org/10.1115/1.4000364兴.

[14] V. Tsisar, C. Schroer, O. Wedemeyer, A. Skrypnik, J. Konys, Long-term corrosion of austenitic steels in flowing LBE at 400 °C and 10−7 mass% dissolved oxygen in comparison with 450 and 550 °C, J. Nucl. Mater. 468 (2016) 305–312, https://doi.org/10.1016/j.jnucmat.2015.09.027.

[15] C. Schroer, O. Wedemeyer, J. Novotny, A. Skrypnik, J. Konys, Long-term service of austenitic steel 1.4571 as a container material for flowing lead–bismuth eutectic, J. Nucl. Mater. 418 (2011) 8–15, https://doi.org/10.1016/j.jnucmat.2011.07.026.

[16] V. Tsisar, C. Schroer, O. Wedemeyer, A. Skrypnik, J. Konys, Corrosion behavior of austenitic steels 1.4970, 316L and 1.4571 in flowing LBE at 450 and 550 °C with 10−7mass% dissolved oxygen, J. Nucl. Mater. 454 (2014) 332–342, https://doi.org/10.1016/j.jnucmat.2014.08.024.

[17] A. Weisenburger, C. Schroer, A. Jianu, A. Heinzel, J. Konys, H. Steiner, G. Müller, C. Fazio, A. Gessi, S. Babayan, A. Kobzova, L. Martinelli, K. Ginestar, F. Balbaud-Célerier, F.J. Martín-Muñoz, L. Soler Crespo, Long term corrosion on T91 and AISI1 316L steel in flowing lead alloy and corrosion protection barrier development: experiments and models, J. Nucl. Mater. 415 (2011) 260–269, https://doi.org/10.1016/j.jnucmat.2011.04.028.

[18] V. Tsisar, O. Yeliseyeva, Oxidation of Armco-Fe and steels in oxygensaturated liquid lead, Mater. High. Temp. 24 (2007) 93–101, https://doi.org/10.3184/096034007×220034.

[19] C. Schroer, V. Koch, O. Wedemeyer, A. Skrypnik, J. Konys, Silicon-containing ferritic/martensitic steel after exposure to oxygen-containing flowing lead–bismuth eutectic at 450 and 550 °C, J. Nucl. Mater. 469 (2016) 162–176, https://doi.org/10.1016/j.jnucmat.2015.11.058.

[20] Y. Kurata, M. Futakawa, Excellent corrosion resistance of 18Cr–20Ni–5Si steel in liquid Pb–Bi, J. Nucl. Mater. 325 (2004) 217–222, https://doi.org/10.1016/j.jnucmat.2003.12.009.

[21] M. Roy, L. Martinelli, K. Ginestar, J. Favergeon, G. Moulin, Dissolution and oxidation behaviour of various austenitic steels and Ni rich alloys in lead-bismuth eutectic at 520 °C, J. Nucl. Mater. 468 (2016) 153–163, https://doi.org/10.1016/j.jnucmat.2015.11.005.

[22] H. Shi, A. Jianu, A. Weisenburger, C. Tang, A. Heinzel, R. Fetzer, F. Lang, R. Stieglitz, G. Müller, Corrosion resistance and microstructural stability of austenitic Fe–Cr–Al–Ni model alloys exposed to oxygen-containing molten lead, J. Nucl. Mater. 524 (2019) 177–190, https://doi.org/10.1016/j.jnucmat.2019.06.043.

[23] J. Ejenstam, P. Szakálos, Long term corrosion resistance of alumina forming austenitic stainless steels in liquid lead, J. Nucl. Mater. 461 (2015) 164–170, https://doi.org/10.1016/j.jnucmat.2015.03.011.

[24] Zhang Jian Zhou Valentyn Tsisar, Aleksandr Skrypnik Olaf Wedemeyer, Carsten Schroer, Effect of Oxygen Concentration in Static Pb-Bi Eutectic on Corrosion Mode of Aluminum-Alloyed Austenitic Steels at 550 °C for 1000 h, Mater. Sci. Forum 1024 (2021) 79–85.

[25] C. Schroer, O. Wedemeyer, J. Konys, Aspects of minimizing steel corrosion in liquid lead-alloys by addition of oxygen, Nucl. Eng. Des. 241 (2011) 4913–4923, https://doi.org/10.1016/j.nucengdes.2011.09.002.

[26] V. Tsisar, S. Gavrilov, C. Schroer, E. Stergar, Long-term corrosion performance of T91 ferritic/martensitic steel at 400 °C in flowing Pb-Bi eutectic with 2 × 10−7 mass% dissolved oxygen, Corros. Sci. 174 (2020), 108852, https://doi.org/10.1016/j.corsci.2020.108852.

[27] C. Schroer, O. Wedemeyer, J. Konys, Gas/liquid oxygen-transfer to flowing lead alloys, Nucl. Eng. Des. 241 (2011) 1310–1318, https://doi.org/10.1016/j.nucengdes.2010.06.047.

[28] J. Lim, A. Mariën, K. Rosseel, A. Aerts, J. Van den Bosch, Accuracy of potentiometric oxygen sensors with Bi/Bi2O3 reference electrode for use in liquid LBE, J. Nucl. Mater. 429 (2012) 270–275, https://doi.org/10.1016/j.jnucmat.2012.06.011.

[29] J. Lim, G. Manfredi, K. Rosseel, A. Aerts, Performance of electrochemical oxygen pump in a liquid lead-bismuth eutectic loop, J. Electrochem. Soc. 166 (2019) E153–E158, https://doi.org/10.1149/2.0711906jes.

[30] J. Lim, G. Manfredi, S. Gavrilov, K. Rosseel, A. Aerts, J. Van den Bosch, Control of dissolved oxygen in liquid LBE by electrochemical oxygen pumping, Sens. Actuators B: Chem. 204 (2014) 388–392, https://doi.org/10.1016/j.snb.2014.07.117.

[31] M.C. Biesinger, B.P. Payne, A.P. Grosvenor, L.W. Lau, A.R. Gerson, R.S. Smart, Resolving surface chemical states in XPS analysis of first row transition metals, oxides and hydroxides: Cr, Mn, Fe, Co and Ni, Appl. Surf. Sci. 257 (2011) 2717–2730, https://doi.org/10.1016/j.apsusc.2010.10.051.

[32] G.C. Allen, S.J. Harris, J.A. Jutson, J.M. Dyke, A study of a number of mixed transition metal oxide spinels using X-ray photoelectron spectroscopy, Appl. Surf. Sci. 37 (1989) 111–134, https://doi.org/10.1016/0169-4332(89)90977-X.

[33] M.A. Langell, J.G. Kim, D.L. Pugmire, W. McCarroll, Nature of oxygen at rocksalt and spinel oxide surfaces, J. Vac. Sci. Technol. A Vac. Surf., Films 19 (2001) 1977–1982, https://doi.org/10.1116/1.1349194.

[34] P. Ernst, N.J. Laycock, M.H. Moayed, R.C. Newman, The mechanism of lacy cover formation in pitting, Corros. Sci. 39 (1997) 1133–1136, https://doi.org/10.1016/S0010-938X(97)00043-7.

[35] P. Ernst, R. Newman, Pit growth studies in stainless steel foils. I. Introduction and pit growth kinetics, Corros. Sci. 44 (2002) 927–941, https://doi.org/10.1016/S0010-938X(01)00133-0.

[36] T.R. McNelley, A.P. Zhilyaev, S. Swaminathan, J. Su, E.S. Menon, Application of EBSD Methods to Severe Plastic Deformation (SPD) and Related Processing Methods, in: A.J. Schwartz, M. Kumar, B.L. Adams (Eds.), Electron Backscatter Diffraction in Materials Science, secondnd ed., Springer, US, Boston, MA, 2009, pp. 277–289.

[37] H.J. Grabke, E.M. Müller-Lorenz, S. Strauss, E. Pippel, J. Woltersdorf, Effects of grain size, cold working, and surface finish on the metal-dusting resistance of steels, Oxid. Met. 50 (1988) 241–254.

[38] V. Tsisar, C. Schroer, O. Wedemeyer, A. Skrypnik, J. Konys, Effect of structural state and surface finishing on corrosion behavior of 1.4970 austenitic steel at 400 and 500 °C in flowing Pb–Bi eutectic with dissolved oxygen, ASME J. Nucl. Rad. Sci. 4 (2018) 41001, https://doi.org/10.1115/1.4040422.

[39] P. Hosemann, D. Frazer, E. Stergar, K. Lambrinou, Twin boundary-accelerated ferritization of austenitic stainless steels in liquid lead–bismuth eutectic, Scr. Mater. 118 (2016) 37–40, https://doi.org/10.1016/j.scriptamat.2016.02.029.

[40] Oksana Klok, Konstantina Lambrinou, Serguei Gavrilov, Erich Stergar, Tom Van der Donck, Shuigen Huang, Bensu Tunca, Iris De Graeve, Influence of plastic deformation on dissolution corrosion of 316L austenitic stainless steel in static, oxygen-poor liquid lead-bismuth eutectic at 500 °C, CORROSION 73 (2017) 1078–1090, https://doi.org/10.5006/2400.

[41] Y. Kurata, Corrosion behavior of cold-worked austenitic stainless steels in liquid lead–bismuth eutectic, J. Nucl. Mater. 448 (2014) 239–249, https://doi.org/10.1016/j.jnucmat.2014.02.006.

[42] K. Lambrinou, E. Charalampopoulou, T. van der Donck, R. Delville, D. Schryvers, Dissolution corrosion of 316L austenitic stainless steels in contact with static liquid lead-bismuth eutectic (LBE) at 500 °C, J. Nucl. Mater. 490 (2017) 9–27, https://doi.org/10.1016/j.jnucmat.2017.04.004.

[43] K.D. Ralston, N. Birbilis, Effect of Grain Size on Corrosion: A Review, 075005-13, Corrosion 66 (2010), 075005, https://doi.org/10.5006/1.3462912.

[44] A. Turnbull, K. Mingard, J.D. Lord, B. Roebuck, D.R. Tice, K.J. Mottershead, N. D. Fairweather, A.K. Bradbury, Sensitivity of stress corrosion cracking of stainless steel to surface machining and grinding procedure, Corros. Sci. 53 (2011) 3398–3415, https://doi.org/10.1016/j.corsci.2011.06.020.

[45] L. Chang, M.G. Burke, F. Scenini, Understanding the effect of surface finish on stress corrosion crack initiation in warm-forged stainless steel 304L in high-temperature water, Scr. Mater. 164 (2019) 1–5, https://doi.org/10.1016/j.scriptamat.2019.01.032.

[46] W. Zhang, K. Fang, Y. Hu, S. Wang, X. Wang, Effect of machining-induced surface residual stress on initiation of stress corrosion cracking in 316 austenitic stainless steel, Corros. Sci. 108 (2016) 173–184, https://doi.org/10.1016/j.corsci.2016.03.008.